

X-ray magnetic circular dichroism and resonant inelastic X-ray scattering explained: role of many-body correlation and mixed-valence fluctuations

Beom Hyun Kim,^{1,*} Sang-Jun Lee,^{2,*} H. Huang,^{2,3} D. Lu,² S. S. Hong,⁴ S. Lee,⁵ P. Abbamonte,⁵ Y. I. Joe,⁶ P. Szypryt,⁶ W. B. Doriese,⁶ D. S. Swetz,⁶ J. N. Ullom,⁶ C.-C. Kao,⁷ J.-S. Lee,^{2,†} and Bongjae Kim^{8,‡}

¹*Center for Theoretical Physics of Complex Systems,
Institute for Basic Science, Daejeon 34126, Republic of Korea*

²*Stanford Synchrotron Radiation Lightsource, SLAC National Accelerator Laboratory, Menlo Park, California 94025, USA*

³*Department of Materials Science and Institute of Optoelectronics, Fudan University, Shanghai 200433, China*

⁴*Department of Materials Science and Engineering,
University of California, Davis, CA 95616, USA*

⁵*Department of Physics and Materials Research Laboratory,
University of Illinois, Urbana, Illinois 61801, USA*

⁶*National Institute of Standards and Technology, Boulder, CO 80305, USA*

⁷*SLAC National Accelerator Laboratory, Menlo Park, California 94025, USA*

⁸*Department of Physics, Kyungpook National University, Daegu 41566, Republic of Korea*

(Dated: December 11, 2024)

X-ray magnetic circular dichroism (XMCD) and resonant inelastic X-ray scattering with magnetic circular dichroism (RIXS-MCD) provide unparalleled insights into the electronic and magnetic dynamics of complex materials. Yet, their spectra remain challenging to interpret due to intricate many-body interactions. Here, we introduce a theoretical framework based on the Anderson impurity model, fully incorporating charge transfer (CT) and core-valence exchange correlation (CVEC) effects. Using epitaxial ferromagnetic $\text{La}_{0.7}\text{Sr}_{0.3}\text{MnO}_3$ film as a model system, we capture elusive spectral features, demonstrating the necessity of CT inclusion for resolving XMCD subpeaks and revealing the profound impact of CVEC on RIXS-MCD spectra. Our approach not only successfully mirrors experimental results but also opens new avenues for exploring spin, orbital, and charge excitations in $3d$ transition metals and other correlated materials.

INTRODUCTION

Strongly correlated electron systems, where electronic, orbital, spin, and structural degrees of freedom interact in complex ways, have been a central focus of condensed matter research for decades [1–9]. The intricate coupling of these degrees of freedom is responsible for the emergence of novel phases, such as the $J_{\text{eff}} = 1/2$ Mott state in iridates [10, 11], unconventional behavior in high- T_c superconductors [12], and the complex magnetic phase diagrams in perovskite heterostructures [1, 2, 13, 14]. Understanding the microscopic origins of these emergent properties requires disentangling the contributions of spin, orbital, and charge dynamics, which often interact in nontrivial ways, particularly in mixed-valence systems.

Distinguishing between the various contributions (*e.g.*, spin vs. orbital) is critical and experimentally challenging, especially in systems where these degrees of freedom are entangled. X-ray magnetic circular dichroism (XMCD) has long been a powerful tool for disentangling spin and orbital contributions in magnetic systems [15–17]. By exploiting the element-specific nature of XMCD, researchers can apply the sum rule to extract spin and

orbital moment values from absorption spectra [17–19]. While XMCD is a valuable tool, it often falls short of fully capturing the complexities of mixed-valence systems and complex correlations. This is because such complexities are due to the many-body interactions that govern the electronic structure of strongly correlated electron systems, particularly in cases where spin-orbit coupling and charge-transfer excitations dominate. In this regard, resonant inelastic X-ray scattering (RIXS), particularly in the form of RIXS-MCD, provides a complementary approach capable of probing both ground and excited state properties [20–27]. It is expected that RIXS-MCD could reveal excitation spectra, including spin, orbital, and charge excitations, offering a more comprehensive picture of the complexities of complex correlations.

Here, we newly establish a comprehensive theoretical approach for understanding XMCD and RIXS-MCD spectral features. We employ the Anderson impurity model (AIM) and incorporate full consideration of charge transfer (CT) and many-body core-valence exchange correlation (CVEC) effects that account for local electronic correlations in both valence and core orbitals and charge fluctuations in the valence orbitals. We found that many-body CVEC plays a significant role in the misinterpretation of XMCD and RIXS-MCD spectra based on simple dipole transitions between occupied core and unoccupied valence states. Further, we reveal that this approach is especially beneficial for interpreting $3d$ transition metals, where XMCD sum-rule analyses can lead to significant

* These authors contributed equally to this work

† jslee@slac.stanford.edu

‡ bongjae@knu.ac.kr

errors due to the coupling of spin and orbital contributions across the L_2 - and L_3 -edges [28–31].

In the following section, to verify our approach, we first demonstrate XMCD and RIXS-MCD measurement on $\text{La}_{0.7}\text{Sr}_{0.3}\text{MnO}_3$ (LSMO) that could be as a model system—a ferromagnetic material with high Fermi-level spin polarization and mixed-valence Mn ions [32–34]. Second, we demonstrate how the approach under full consideration of CT and many-body CVEC works on the LSMO case. Finally, we elaborate that our combined theoretical and experimental approach provides deeper insights into XMCD and RIXS-MCD processes, particularly for light $3d$ transition-metal systems, offering a complete and robust framework for studying other correlated materials.

ANDERSON IMPURITY MODEL

To gain microscopic insights into the XMCD and RIXS-MCD spectra, we employ the configuration interaction (CI) calculation based on the Anderson impurity model (AIM). Here, the CT effect of ligand orbitals are considered as a bath. Analogous to conventional CI calculations [35], we incorporate five ligand (bath) orbitals with identical energy e_L , whose symmetric properties are the same as those of five d orbitals. For the overlap integrals, we assume σ -type (π -type) overlaps between $3d$ and bath orbitals with the e_g (t_{2g}) symmetry. In line with the CI approach, we assign overlap strength of $\sqrt{3}V_{pd\sigma}$ for e_g orbitals and $2V_{pd\pi}$ for t_{2g} orbitals, where $V_{pd\sigma}$ and $V_{pd\pi}$ denotes the interatomic matrix elements for σ and π bonds, respectively.

Following is the full AIM Hamiltonian we consider:

$$H = H_d + H_c + H_{dc} + H_L + H_t, \quad (1)$$

where

- H_d : Hamiltonian of Mn $3d$ valence orbitals characterized by the cubic crystal field ($10Dq$), spin-orbit coupling (λ), long-range magnetic field h , and Coulomb interactions (U_{dd} , F_{dd}^2 , F_{dd}^4).
- H_c : Hamiltonian of Mn $2p$ core orbitals characterized by the spin-orbit coupling (λ_c) and energy level (e_c).
- H_{dc} : Hamiltonian of core-valence exchange correlations characterized by Slater-Condon parameters (U_{pd} , F_{pd}^2 , G_{pd}^1 , G_{pd}^3).
- H_L : Local energy of ligand (bath) orbital characterized by the energy level e_L .
- H_t : Hopping Hamiltonian between valence $3d$ and ligand (bath) orbitals characterized by $V_{pd\sigma}$ and $V_{pd\pi}$.

Slater-Condon parameters (F_{dd}^2 , F_{dd}^4 , F_{pd}^1 , G_{pd}^1 , G_{pd}^3) are typically set at 80% of Hatree-Fock values (atomic values) [36]. In our LSMO calculation, we adopt the arithmetic mean of Mn^{4+} and Mn^{3+} atomic values for

these parameters, including the spin-orbit coupling parameter of Mn valence orbitals λ . The spin-orbit coupling parameter of Mn core orbitals λ_c is selected for fitting the experimental XAS splitting of L_2 and L_3 edges optimally. The Coulomb repulsion parameters U_{dd} and U_{pd} are defined as $U_{dd} = F_{dd}^0 - \frac{2}{63}(F_{dd}^2 + F_{dd}^4)$ and $U_{pd} = F_{pd}^0 - \frac{1}{15}G_{pd}^1 - \frac{3}{70}G_{pd}^3$, respectively [37]. As a common approximation, We set U_{pd} to be 1 eV higher than U_{dd} [35]. The CT energy Δ in d^3 atomic multiplets is defined as the difference between the center of energies of d^3 and d^4L^1 , where L refers to the ligand (bath) hole orbitals. This is obtained as $\Delta = E(d^4L^1) - E(d^3) = 3U_{dd} + 6U_{pd} - \epsilon_L$ assuming all ligand (bath) hole orbitals have the same energy of ϵ_L . In the calculation, ϵ_L is automatically set according to Δ , U_{dd} , and U_{pd} values. To incorporate the magnetic ordering effect of LSMO, we apply a magnetic field of $\mu_B h = 0.01$ eV, corresponding to the mean-field from neighboring ferromagnetic spins. The remaining parameters are adjusted to fit the experimental spectra. The specific parameters used are presented in Table I.

In the metallic LSMO system, description of the mixed-valence nature of Mn ions is crucial but very tricky. Here, we consider the CT effect from the ligand (bath) states. We begin with the initial d^3L^0 configurations, where L represents the ligand (bath) hole orbital, and subsequently include full CT states, ranging from d^4L^1 to $d^{10}L^7$ configurations. This approach is markedly different from the conventional approach for the mixed valence, where the weighted sum of spectra from each ions of Mn^{3+} and Mn^{4+} is considered. As we will demonstrate below, our approach with full CT consideration delivers critically improved description of the experimental spectra. The AIM is solved applying the exact diagonalization based on the Lanczos method [38], and we calculated the ground state and its energy. The physical parameters, listed in Table I, are optimized to ensure that the calculated spectra closely resemble the experimental ones [see supplementary material for the details on the CT effects].

In the CI approach, the ground multiplet state is approximately an admixture of states with d^3L^0 , d^4L^1 , and d^5L^2 configurations, reflecting the mixed-valence nature of the system. Specifically, our obtained ground state wave function can be approximated as 30%, 49%, and 19% configurations of d^3L^0 , d^4L^1 , and d^5L^2 states, respectively. Our AIM captures essential electronic features qualitatively and we confirm our CI calculation effectively captures the mixed-valence fluctuations in LSMO systems. Based on our ground state, we calculate the XAS and RIXS spectra. The details on XAS and RIXS calculations are described in supplementary materials.

TABLE I. Physical parameters for the Anderson impurity model in the eV unit.

$10Dq$	λ	F_{dd}^2	F_{dd}^4	λ_c	F_{pd}^2	G_{pd}^1	G_{pd}^3	Δ	U_{dd}	U_{pd}	$V_{pd\sigma}$	$V_{pd\pi}$
1.5	0.0478	9.3723	5.8794	7.500	5.7508	4.2864	2.4382	2	5	6	-2	1

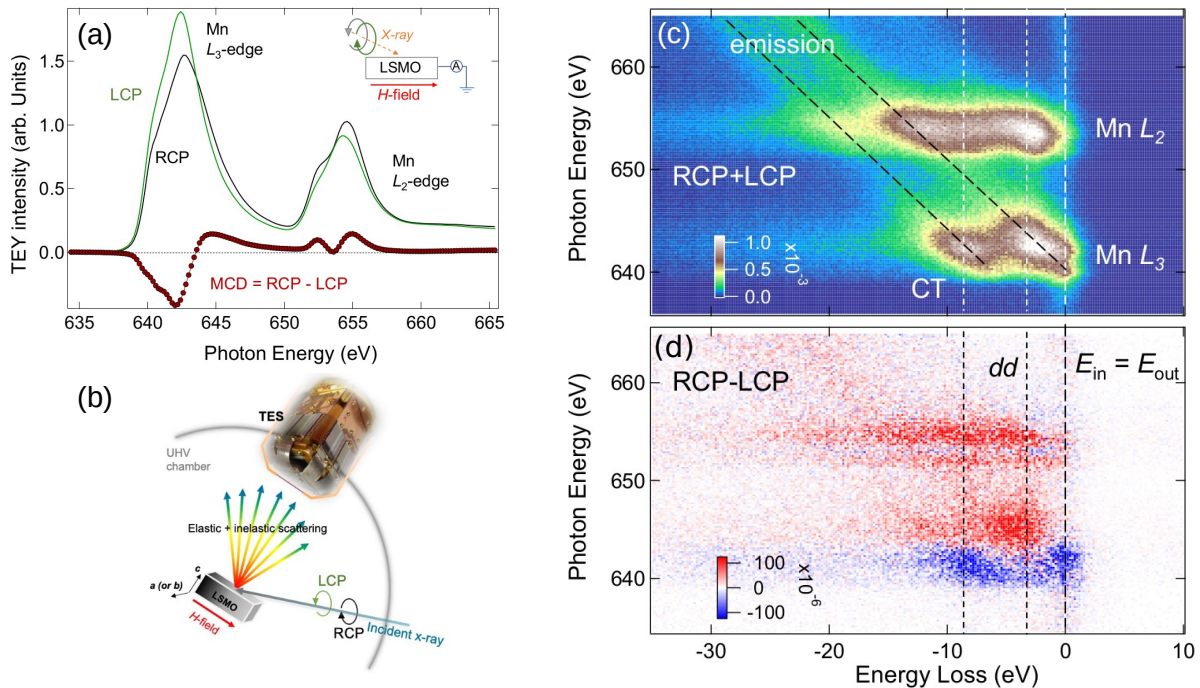


FIG. 1. (a) X-ray absorption spectroscopy (XAS) and magnetic circular dichroism (MCD) spectra of $\text{La}_{0.7}\text{Sr}_{0.3}\text{MnO}_3$ (LSMO) measured in the total electron yield (TEY) mode. The black and green curves are the absorption spectra of right circular polarization (RCP) μ_+ and left circular polarization (LCP) μ_- , respectively. The curve with circle symbols is the MCD spectrum ($\Delta\mu$). The inset in (a) shows the experimental configuration for the MCD measurement. The symbol \AA denotes an ammeter to measure the TEY. (b) Schematic drawing of the resonant inelastic X-ray scattering (RIXS) measurement set-up using a transition-edge-sensor (TES) spectrometer. (c) A RIXS map as functions of the energy loss ($\Delta E = E_{\text{out}} - E_{\text{in}}$) and the photon energy (E_{in}) of the LSMO measured by the TES spectrometer. The map represents the sum of RIXS intensities for the RCP and LCP incident photons. (d) A RIXS-MCD map obtained by differing two RIXS maps measured with RCP and LCP incident photons. Along the dashed line around $-5 < \Delta E < -3$ eV, a strong dichroic intensity was observed at $E_{\text{in}} \sim 644.6$ eV, which corresponds to the dd -excitation.

EXPERIMENTAL RESULTS

We perform the X-ray absorption spectroscopy (XAS) of epitaxial LSMO films with two polarizations, right circular polarization (RCP) and left circular polarization (LCP) (see the detail in Methods section). The XMCD spectrum ($\Delta\mu$) is generated as the difference of the two XAS spectra obtained with RCP (μ_+) and LCP (μ_-). As shown in Fig. 1(a), obtained spectra are well consistent with the previous reports [39, 40]. At the L_3 -edge, $\Delta\mu$ exhibits two dichroism features at around 642.1 eV and 644.6 eV, with a 2.5 eV energy difference. Similarly, at the L_2 -edge, $\Delta\mu$ displays two features at around 652.5 eV and 655.0 eV, indicating the same energy difference. This correlation suggests a connection between the dichroism features of the L_3 -edge and those of the L_2 -edge, which

becomes uncovered later.

Considering the magnetic exchange splitting of the $3d$ valence band between up and down spins, the sign of XMCD between the L_3 and L_2 edges is typically opposite [15, 17–19, 41], as observed in the two main XMCD peaks at 642.1 eV for the L_3 edge and 652.5 eV for the L_2 edge [see Fig. 1(a)]. However, the other subpeak at 644.6 eV for the L_3 edge and 655.0 eV for the L_2 edge exhibit the same sign of XMCD. This discrepancy, along with the overshoot observed at the L_3 -edge XMCD resembling the diffused moment behavior reported in Ref. 28, leads to a strong overestimation and underestimation of the orbital and spin moment, respectively, when applying the sum-rule. This representatively shows the limitations of XMCD sum-rules [42–45], particularly in exploring orbital angular momentum, and raises fun-

damental questions on the application of the sum-rule. Understanding the origin of this sign-reversal behavior and identifying the legitimate regime of the sum-rule is essential. A comprehensive analysis of XMCD spectra calls for microscopic theories to determine the complex multiplet structure of Mn $3d$ orbitals.

We further explore RIXS and RIXS-MCD spectra [see the detail in Methods section]. By monitoring ΔE for each E_{in} through RIXS measurement [see Fig. 1(b) and (c)], we generate a map of LSMO as functions of ΔE and E_{in} by summing the maps measured with RCP and LCP at $T = 25$ K. Figure 1(c) is a magnified view of the RIXS map over the Mn L -edge region, where we identify quasi-elastic, dd -excitation, CT, and fluorescence signals. The quasi-elastic ($\Delta E \sim 0$) includes not only the elastic but also phonon and magnon contributions due to the spectrometer's energy resolution of 1.5 eV [21, 46, 47]. Mn's dd -excitation ($\Delta E \sim -3$ eV) and CT (-10 eV $< \Delta E < -3$ eV) are well pronounced [see the theoretical analysis in next section]. The fluorescence appears along the diagonal direction guided with dashed lines in Fig. 1(c).

The RIXS-MCD map, obtained from the difference of two RIXS maps with RCP and LCP incident photons, is presented in Fig. 1(d). We observe the strong dependency of the RIXS-MCD map on the incident photon energy, showing the separation of RCP and LCP dominant spectra. Positive and negative RIXS-MCD signals are extended over the loss energy when the incident energy is at around the XMCD absorption peaks. It supports that the overall fluorescence features of XMCD correspond well to the XMCD features measured using the total electron yield (TEY) mode at the Mn $L_{2,3}$ edges.

Given that the Fermi-level spin polarization of LSMO is highly pronounced [32–34], both elastic and inelastic processes are influenced by its magnetically polarized behavior. Interestingly, we observe that the XMCD feature at $E_{\text{in}} \sim 644.6$ eV is more prominent in the RIXS-MCD compared to other excitations, which still correspond to the total MCD signal based on TEY measurements. The energy loss value of this feature suggests that its origin is Mn's dd -excitation, opening up possibilities for further discussion on the orbital moment investigated using the RIXS-MCD approach.

XMCD SPECTRA

As shown in Figs. 2(a) and (b), we obtain the theoretical XAS and XMCD spectra which are highly consistent with experimental ones. To ensure comprehensive understanding, we investigate the XMCD behaviors focusing on the two key effects: CT and CVEC.

One of the most evident difference between our model and conventional approaches is the treatment of CT effects. Conventionally, the CT states are restricted into

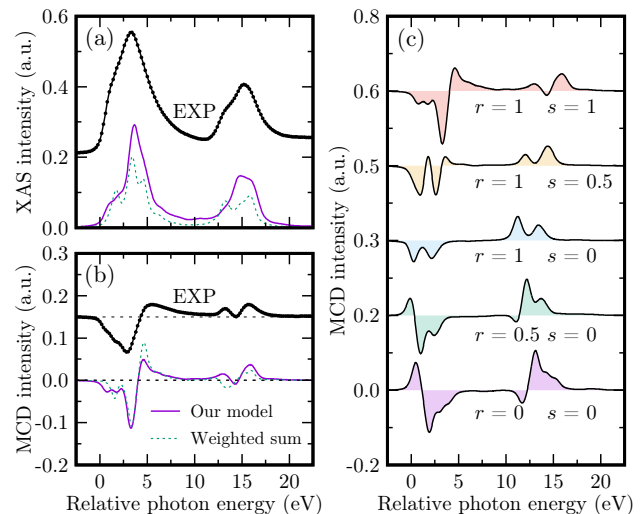


FIG. 2. Theoretical spectra of (a) X-ray absorption spectroscopy (XAS) and (b) magnetic circular dichroism (MCD) of LSMO calculated by adding and subtracting the absorption spectra with right and left circular polarizations. The solid magenta lines correspond to the results from our model, which include full charge transfer (CT) states with configurations ranging from d^4L^1 to $d^{10}L^7$, where L represents a ligand (bath) hole orbital. The dotted green lines show the weighted sum of 30% contribution from Mn $^{4+}$ spectra and 70% contribution from Mn $^{3+}$ spectra, calculated using the CTM4XAS software with partial CT states, i.e., d^4L^1 states for Mn $^{4+}$ and d^5L^1 states for Mn $^{3+}$ [36]. (c) The XMCD results for various CVEC strengths and hopping integrals between valence $3d$ and ligand (bath) orbitals. The Slater-Condon parameters are scaled by s as $F_{pd}^2 = 5.7508 \times s$, $G_{pd}^1 = 4.2864 \times s$, and $G_{pd}^3 = 2.4382 \times s$ eV, and the scale parameter r is defined as $V_{pd\sigma} = -2 \times r$ and $V_{pd\pi} = 1 \times r$ eV. Other parameters are presented in Table I.

only major state, $d^{n+1}L^1$ configuration [35, 36]. Then the spectra from mixed valence ions is obtained from the spectra of each ionic states separately – Mn $^{3+}$ and Mn $^{4+}$ for LSMO. Then one simply performs the weighted sum of two spectra upon their mixing ratio. This treatment successfully depict the main features of the experimental XMCD spectra in many cases [48, 49]. However, these conventional procedures notoriously fail to simulate the experimental XMCD spectra of highly metallic LSMO (see Fig. S3 in supplementary materials). Specifically, two important features, the extended subpeak spectra in the L_3 -edge for the relative photon energy of around 0 – 2 eV, and positive peak in the L_2 -edge for the 13 – 14 eV regime, are not accounted in the conventional approaches. (See the dotted data of Fig. 2(b)) (see also supplementary materials).

In our AIM model, effect of CT is treated with strong hopping on top of small CT energy, and full consideration of CT enables us to capture simultaneously the valence fluctuations of Mn d electrons ranging from d^3 to d^{10} . Hence, our ground multiplet state well accounts for the

CT nature beyond $d^{n+1}L^1$. The dynamic charge fluctuation is better treated in our model than the conventional partial CT approaches, and as shown in Fig. 2(a) and (b), we successfully described the key features of the experimental XAS and MCD spectra. This result demonstrates the importance of the full CT treatment, hence, the inclusion of the appropriate mixed-valence nature of Mn ions, in the comprehensive account of the XAS and XMCD spectra of metallic LSMO.

Now we include many-body correlation of core-valence states and systematically investigate the XMCD spectral evolution as functions of the CT and CVEC effects together. To this end, here, we adjust the hopping strengths and Slater-Condon parameters of core-valence orbitals using two scale parameters r and s , such that $V_{pd\sigma} = -2 \times r$ and $V_{pd\pi} = 1 \times r$ eV, and $F_{pd}^2 = 5.7508 \times s$, $G_{pd}^1 = 4.2864 \times s$ and $G_{pd}^3 = 2.4382 \times s$ eV. Hence, r and s act as a scaling factor for each CT and CVEC channel (Fig. 2(c)). When both effects are absent ($r = 0, s = 0$), the L_3 -edge XMCD spectra consist of a main peak with a negative sign and a subpeak with a positive sign, and corresponding L_2 -edge has the opposite composition, a main peak with a positive and subpeak with a negative sign as expected [15, 17–19, 41]. With excluding the CVEC effect ($s = 0$), we vary the strength of the CT channel. As we increase the hopping strengths ($r = 0.5$), the positive (negative) subpeak in the L_3 -edge (L_2 -edge) progressively diminishes, and the negative (positive) main peak bifurcates to give two-peak structures. When full CT effects are included ($r = 1$), the subpeak signatures are all gone, and we observe two negative peaks in the L_3 -edge and two positive peaks in the L_2 -edge, both evolved from the main peak in the ($r = 0, s = 0$) case (Fig. 2(c)).

The fine structure of XMCD peaks for the $r = 0, s = 0$ case depends solely on the *local* correlation effects of Mn-3d orbitals, such as crystal field energy and exchange Coulomb interactions, characterized by F_{dd}^2 and F_{dd}^4 . Upon increasing r , the fine structure smoothed out. This indicates that strong p - d hopping, which is due to the metallic nature of Mn ions, effectively screens the detailed local effects. In the absence of the CVEC, the L_3 -edge (L_2 -edge) XAS spectra can be directly interpreted with the simple dipole transition picture: excitations from the occupied core $p_{3/2}$ ($p_{1/2}$) orbitals to the unoccupied valence 3d orbitals.

Given that the spin-polarized ground state predominantly comprises the multiplet state with the $t_{2g\uparrow}^3$ configuration ($|t_{2g\uparrow}^3\rangle$), we investigate its dipole transition behaviors. Due to dipole selection rules, the transition from $p_{3/2,+3/2}$ ($p_{3/2,-3/2}$) to $\varphi_{x^2-y^2\uparrow}$ ($\varphi_{x^2-y^2\downarrow}$) orbitals of RCP (LCP) photons exhibits maximum amplitude at the L_3 edge. Conversely, the transition from $p_{1/2,+1/2}$ ($p_{1/2,-1/2}$) to $\varphi_{x^2-y^2\downarrow}$ ($\varphi_{x^2-y^2\uparrow}$) orbitals shows maximum amplitude at the L_2 edge, as illustrated in Fig. 3(a) and (b). Additionally, the transition from $p_{3/2,-3/2}$ to $\varphi_{xy\downarrow}$

orbitals of LCP photons contributes more significantly than the transition from $p_{3/2,+1/2}$ to $\varphi_{xy\downarrow}$ orbitals of RCP photons at the L_3 edge. Moreover, the transition from $p_{1/2,\pm 1/2}$ to $\varphi_{xy\downarrow}$ orbitals of LCP photons is forbidden at the L_2 edge. These spin and orbital dependencies of dipole transitions lead to the observed dichroism in Mn ions.

To identify the microscopic contributions, we calculate the partial excitation density (PED) of the final states derived from $|t_{2g\uparrow}^3\rangle$ through dipole transitions from core $2p$ to valence t_{2g} and e_g orbitals ($D_{\pm}^{t_{2g}}|t_{2g\uparrow}^3\rangle$ and $D_{\pm}^{e_g}|t_{2g\uparrow}^3\rangle$, respectively). The detailed calculations can be found in the supplementary materials. The results are presented in Fig. 3(c) and (d).

The peaks of PED for $D_{\pm}^{t_{2g}}|t_{2g\uparrow}^3\rangle$ appear at the eigenenergies of the final multiplet states, which consist of $t_{2g\uparrow}^3 t_{2g\downarrow}^1 c^1$ configurations for $D_{\pm}^{t_{2g}}|t_{2g\uparrow}^3\rangle$, and $t_{2g\uparrow}^3 e_{g\uparrow}^1 c^1$ and $t_{2g\uparrow}^3 e_{g\downarrow}^1 c^1$ configurations for $D_{\pm}^{e_g}|t_{2g\uparrow}^3\rangle$. Here, c denotes the core $2p$ hole. For $r = 1, s = 0$, the multiplet states with $t_{2g\uparrow}^3 t_{2g\downarrow}^1 c^1$ and $t_{2g\uparrow}^3 e_{g\uparrow}^1 c^1$ configurations exhibit peaks at around 0.2 eV at the L_3 edge and 11.4 eV at the L_2 edge of relative photon energy. Additionally, the multiplet states with the $t_{2g\uparrow}^3 e_{g\downarrow}^1 c^1$ configuration show main peaks at around 2.2 eV at the L_3 edge and 13.3 eV at the L_2 edge, with subpeaks at around 0.2 eV at the L_3 edge and 11.4 eV at the L_2 edge. Thus, the negative (positive) XMCD peak at around 2.2 eV (13.3 eV) at the L_3 (L_2) edge can be attributed to the contribution of multiplet states with $t_{2g\uparrow}^3 e_{g\downarrow}^1 c^1$ derived from the dipole transition from $p_{3/2}$ ($p_{1/2}$) to $e_{g\downarrow}$. The negative (positive) XMCD peak at around 0.2 eV (11.4 eV) results from the sum of positive (negative) and negative (positive) contributions of the dipole transition from $p_{3/2}$ ($p_{1/2}$) to $e_{g\uparrow}$ and from $p_{3/2}$ ($p_{1/2}$) to $t_{2g\downarrow}$, respectively.

The ground multiplet state also includes the CT state with a $t_{2g\uparrow}^3 e_{g\uparrow}^1 L_{e_g\uparrow}$ contribution, where $L_{e_g\uparrow}$ denotes a ligand hole state with e_g orbital symmetry and up spin state. We find that the PED behaviors for $D_{\pm}|t_{2g\uparrow}^3 e_{g\uparrow}^1 L_{e_g\uparrow}\rangle$ are almost identical to those for $D_{\pm}|t_{2g\uparrow}^3\rangle$ [see supplementary materials for details]. The XMCD attributed to Mn³⁺ also supports the two-peak structures observed in the spectra.

The two-peak structures for $r = 1, s = 0$ is a reflection of the electronic structures [see supplementary materials], where the large and small peak corresponds to the unoccupied Mn-3d bands at around 2 and 4 eV, respectively. The former is the mixture of the t_{2g} and e_g , but the latter is mainly of the e_g character. Here, we note that the conventional sum-rule analysis, which separately treats L_2 - and L_3 -edge with *circa* one-body picture, remains valid regardless of the CT effect as long as the many-body CVEC are absent.

Now we explore the behaviors of XMCD spectra upon the inclusion of the CVEC. Most importantly, the response of the L_3 - and L_2 -edge XMCD spectra are totally

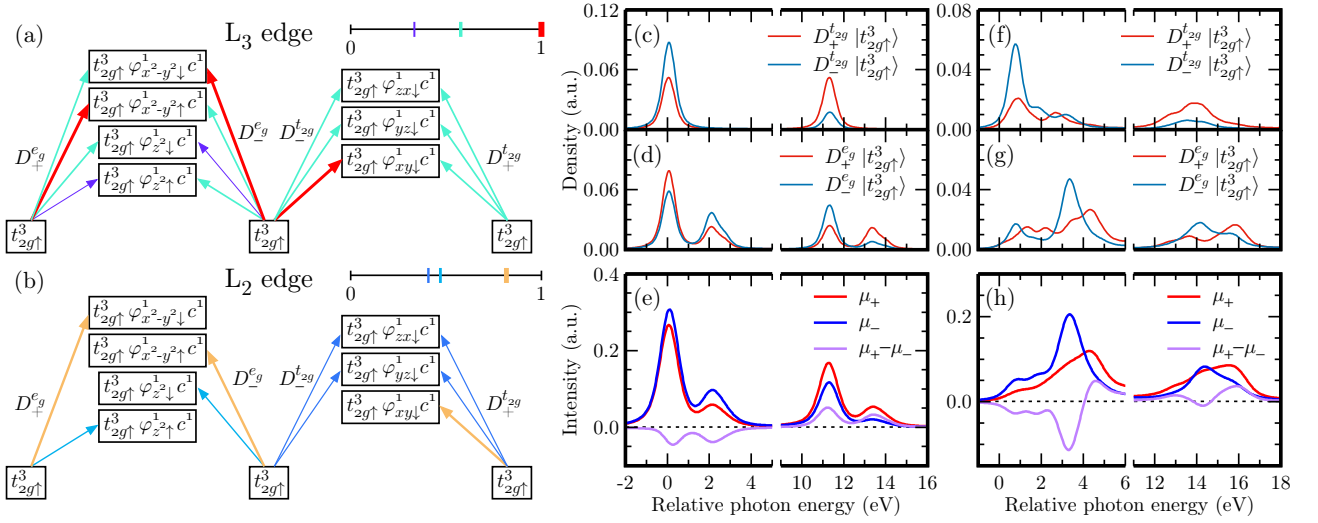


FIG. 3. Schematic diagrams of dipole transitions from the $|t_{2g}^3 \uparrow\rangle$ state at the (a) L_3 and (b) L_2 edges. $D_+^{t_{2g}}$ and $D_+^{e_g}$ ($D_-^{t_{2g}}$ and $D_-^{e_g}$) denote the dipole transition operators for right (left) circularly polarized photons from core $2p$ to valence t_{2g} and e_g orbitals, respectively. The thickness of arrows indicates the strength of dipole transitions, with relative values marked at the top-right horizontal lines. The partial excitation distribution (PED) behaviors of multiplet states derived from $|t_{2g}^3 \uparrow\rangle$ by the dipole operators $D_+^{t_{2g}}$, $D_-^{t_{2g}}$, $D_+^{e_g}$, and $D_-^{e_g}$ when the scale parameter s is 0 for (c) & (d), and 1 for (f) & (g). The theoretical L_3 -edge X-ray magnetic circular dichroism (XMCD) spectra for (e) $s = 0$ and (h) $s = 1$. The scale parameter is defined as $F_{pd}^2 = 5.7508 \times s$, $G_{pd}^1 = 4.2864 \times s$, and $G_{pd}^3 = 2.4382 \times s$ eV. Other parameters are presented in Table I.

different upon the CVEC effect. As s is increased from 0 to 1, in the L_2 -edge sector, the positive two-peak structures remain robust despite the changes in the weight, which is transferred from the lower to upper peak. However, in the L_3 sector, the inclusion of CVEC dramatically alters the overall shape of the spectra. Positive spectra emerge in the upper parts of the L_3 edge, eventually evolving into the positive peak in the L_3 edge, which corresponds to the XMCD peak at around 644.6 eV in the experiments. The two negative peaks rearrange into one negative peak with subpeak structures. Now, the XMCD spectra *cannot* be simply interpreted as the dipole transition between occupied core and unoccupied valence electronic bands, and the conventional analysis on the XMCD sign, hence the sum-rule, is no longer valid in the presence of the CVEC. The full inclusion of CT and CVEC is needed to simulate the experimental XMCD spectra (Fig. 2(b)).

One can obtain the microscopic insight from the PED behaviors for the full inclusion of CT and CVEC effects ($r = 1, s = 1$) case. Figures 3(f) and (g) present the PED behaviors for $D_{\pm}^{t_{2g}} |t_{2g}^3 \uparrow\rangle$ and $D_{\pm}^{e_g} |t_{2g}^3 \uparrow\rangle$, respectively. The CVEC arises from the atomic electron-electron correlations between core $2p$ and valence $3d$ orbitals, allowing exchanges between $p_{1/2}$ and $p_{3/2}$ core holes along with simultaneous exchanges among valence d orbitals. This leads to a fine structure of the final multiplet states in the XAS process. Consequently, the PEDs are much extended, and the XMCD spectra exhibit complex behaviors.

The dominant negative peak at around 3.3 eV and the positive one at 4.4 eV in the L_3 edge XMCD can be attributed to the dipole transition from $p_{3/2}$ to e_g orbitals. And we see that the L_2 -edge XMCD spectra near 14.3 eV are almost compensated by positive and negative contributions from the dipole transitions from $p_{1/2}$ to t_{2g} and e_g orbitals, respectively, and the positive peak around 13.1 eV mainly originated from the dipole transition from $p_{1/2}$ to t_{2g} orbitals. These observations highlight the intricate effects of CVEC on the PED, hence, on the XMCD spectra, emphasizing the need for a detailed analysis of these interactions to understand the underlying electronic transitions.

For the microscopic understanding of full CT effects, we investigate the PED behaviors for the dipole transition for two ligand hole state $D_{\pm} |t_{2g}^3 \uparrow e_{g\uparrow}^2 L_{e_g\uparrow}^2\rangle$ [see supplementary materials]. Unlike the cases for $|t_{2g}^3 \uparrow\rangle$ and $|t_{2g}^3 \uparrow e_{g\uparrow}^1 L_{e_g\uparrow}^1\rangle$, the dipole transition from $p_{3/2}$ and $p_{1/2}$ to $e_{g\uparrow}$ orbitals is prohibited because all $e_{g\uparrow}$ orbitals are fully occupied. Consequently, the PED for $D_{\pm} |t_{2g}^3 \uparrow e_{g\uparrow}^2 L_{e_g\uparrow}^2\rangle$ exhibit different characteristics from those observed in the $|t_{2g}^3 \uparrow\rangle$ and $|t_{2g}^3 \uparrow e_{g\uparrow}^1 L_{e_g\uparrow}^1\rangle$ cases. We clearly see in Fig. 3(c), for $r = 1, s = 0$, the negative (positive) contributions to the XMCD at around 0.2 (11.4) eV are generated by the dipole transition from $p_{3/2}$ ($p_{1/2}$) to $e_{g\uparrow}$ orbitals. This remains the same even for the full inclusion of CVEC effect, $r = 1, s = 1$. Therefore, we ascertain the importance of the full CT inclusion, which provides complete description of the XMCD behaviors – notably the negative XMCD spectra at the L_3 edge near 0.2 eV

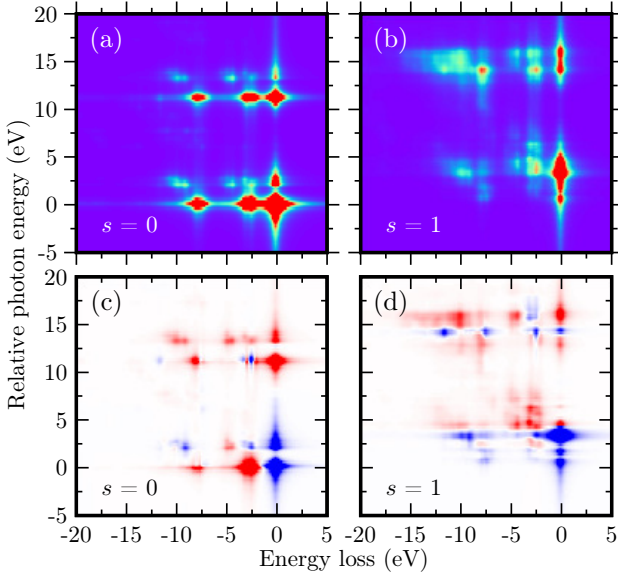


FIG. 4. Theoretical resonant inelastic X-ray scattering (RIXS) map for depending on the scale parameter (s) of the CVEC channel (a) $s = 1, s = 0$ and (b) $r = 1, s = 1$, and their MCD map for (c) $r = 1, s = 0$ and (d) $r = 1, s = 1$.

and the positive XMCD peak at the L_2 edge near 13.1 eV that conventional approach with sole $d^{n+1}L^1$ inclusion cannot achieve. Especially for the systems with significant mixed-valence fluctuations, our findings underscore the importance of full CT effects consideration for the accurate description of the XMCD spectra.

RIXS-MCD SPECTRA

Now we analyze the RIXS and RIXS-MCD spectra, where the importance of the CVEC is further emphasized. We calculate these spectra assuming the incident photon has the LCP or RCP as in the experimental X-ray geometry setup as shown in Fig. 1(b) [see the supplementary material for the calculation details]. In Figs. 4(a)–(d), we present the calculated RIXS and RIXS-MCD maps as functions of incident photon energy and outgoing photon energy loss for the cases of the absence ($s = 0$) and presence of the CVEC ($s = 1$). We find that our calculation with full consideration of the CVEC in the strong d - p hopping regime, shown in Fig. 4(b) and (d), successfully reproduce the experimental RIXS and RIXS-XMCD in Fig. 1(c) and (d).

In both $s = 0$ and 1 cases, the calculations yield identical multiplet structures for the initial and final states in the RIXS process, which shows that the CVEC is inert unless the core holes are populated. Consequently, the positions of RIXS and RIXS-MCD peaks with respect to the energy loss remain the same.

However, the details of the peak structures, such as the sign and intensities, exhibit markedly different behaviors

depending on the CVEC strengths. The CVEC strongly affect the intermediate states of the RIXS process, and split them into finer structures, thereby modifying the effective selection rule for a given photon energy. As a result, when the CVEC effect is included, the RIXS-MCD maps extend over wider ranges of the incident photon energy. Note that the negative L_3 edge at the elastic part shifts downward while the positive portion at the inelastic part moves upward [see Fig. 4(c) and (d)].

For a comprehensive analysis on the RIXS-MCD spectra, we explore the transitions of ground multiplet configurations during the absorption and emission processes in RIXS. Figures 5(a) and (b) illustrate the transitions starting from the initial configurations $t_{2g\uparrow}^3$ and $t_{2g\uparrow}^3 e_{g\uparrow}^1 L_{e_g\uparrow}^1$. As a result, the final states derived from $|t_{2g\uparrow}^3\rangle$ are mainly attributed to the states with $t_{2g\uparrow}^3$, $t_{2g\uparrow}^2 t_{2g\downarrow}^1$, $t_{2g\uparrow}^2 e_{g\uparrow}^1$, and $t_{2g\uparrow}^2 e_{g\downarrow}^1$ configurations. Similarly, the final states derived from $|t_{2g\uparrow}^3 e_{g\uparrow}^1 L_{e_g\uparrow}^1\rangle$ are mainly attributed to the states with $t_{2g\uparrow}^3 e_{g\uparrow}^1 L_{e_g\uparrow}^1$, $t_{2g\uparrow}^2 e_{g\uparrow}^1 t_{2g\downarrow}^1 L_{e_g\uparrow}^1$, $t_{2g\uparrow}^2 e_{g\uparrow}^2 L_{e_g\uparrow}^1$, and $t_{2g\uparrow}^2 e_{g\uparrow}^1 e_{g\downarrow}^1 L_{e_g\uparrow}^1$ configurations. With these setups, we can calculate the microscopic PED behaviors of the relevant final states involved in the RIXS-MCD process as shown in Figs. 5(c) and (d).

We observe that the local dd excitations primarily contribute to the RIXS spectra for -1 – 5 eV, while CT excitations become more prominent for -6 – 15 eV, possibly due to enhanced Coulomb interactions. Additionally, the RIXS-MCD peaks above 1 eV for both $s = 0$ and 1 cases are mainly attributed to the excited states with $t_{2g\uparrow}^2 e_{g\uparrow}^1$, $t_{2g\uparrow}^2 e_{g\downarrow}^1$, $t_{2g\uparrow}^2 e_{g\uparrow}^2 L_{e_g\uparrow}^1$, and $t_{2g\uparrow}^2 e_{g\uparrow}^1 e_{g\downarrow}^1 L_{e_g\uparrow}^1$ configurations. The peak positions of their PED spectra are well matched with those of RIXS-MCD spectra, and we can clearly identify the origins of the multiple features.

Here, we want to emphasize that the detailed behaviors show a strong dependency on the relative photon energy ω_{rel} and CVEC effects. For instance, the RIXS-MCD spectra without the CVEC effect, $s = 0$, and for $\omega_{rel} = 0.2$ eV exhibit positive peaks at around -3 eV of energy loss, while for $s = 0$ and $\omega_{rel} = 2.2$ eV they show negative peaks and additional positive peaks at around -5 eV of energy loss. If one includes the full CVEC effect, $s = 1$, and for $\omega_{rel} = 3.4$ eV, negative peaks emerge at about -2.5 and -4.3 eV in the RIXS-MCD spectra. In contrast, positive three peaks shown at approximately -2.5 , -3.0 , and -4.3 eV, which is consistent with the peak positions of PED of the $t_{2g\uparrow}^2 e_{g\downarrow}^1$ ($t_{2g\uparrow}^2 e_{g\uparrow}^1 e_{g\downarrow}^1 L_{e_g\uparrow}^1$) configuration for $s = 1$ and $\omega_{rel} = 4.4$ eV [see Fig. 5(e) and (f)]. These observations directly support that CVEC effect predominantly determines the energies and symmetries of the intermediate states, which eventually structures the RIXS-MCD selections. Here, we clearly demonstrated our model can identify the details of the signals, and the inelastic component measurement via RIXS-MCD would be considerable to be an alternative way for exploring the microscopics of the

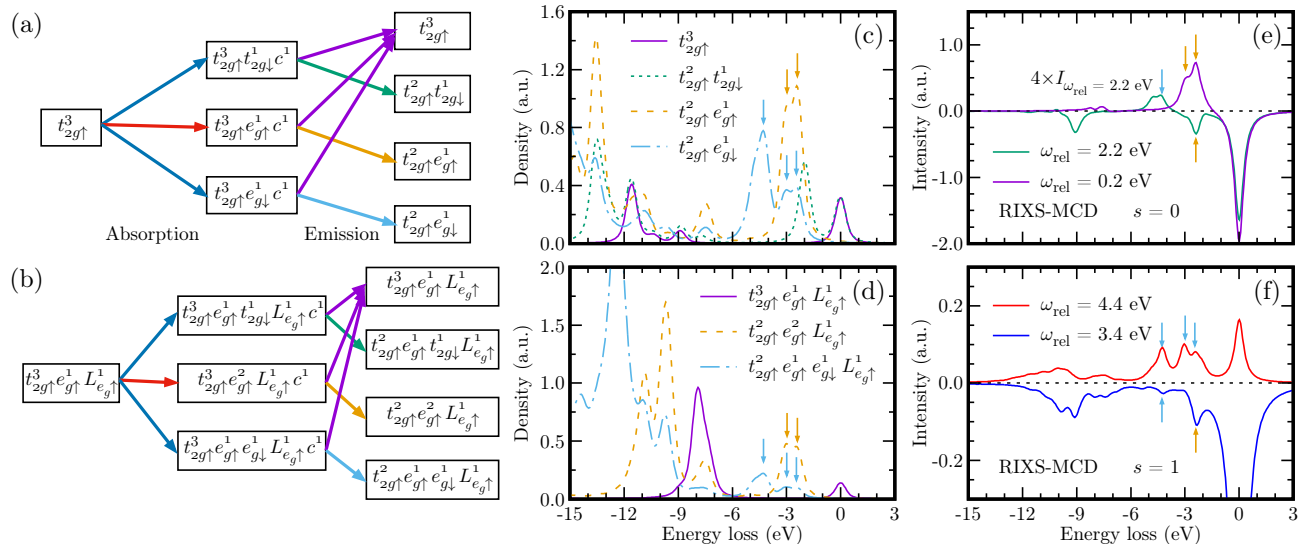


FIG. 5. Schematic diagram of the resonant inelastic X-ray scattering (RIXS) process from relevant ground configurations: (a) t_{2g}^3 and (b) $t_{2g}^3 e_g^1 L_{e_g}^1$. Here, $L_{e_g}^1$ denotes a ligand (bath) hole orbital with e_g orbital symmetry and \uparrow spin state. The partial excitation distribution (PED) behaviors of final states derived from initial (c) $|t_{2g}^3\rangle$ and (d) $|t_{2g}^3 e_g^1 L_{e_g}^1\rangle$ states. The theoretical RIXS-MCD spectra when the relative photon energies of incident X-ray are (e) 0.2 and 2.2 eV for $s = 0$, and (f) 3.4 and 4.4 eV for $s = 1$. These energies are consistent with the peak positions of the measured XMCD spectra. Colored arrows indicate the peak positions of PED spectra drawn with corresponding colors. Other parameters are presented in Table I.

complex systems.

CONCLUSION

In conclusion, by employing AIM calculation that fully accounts for the CT and many-body CVEC, we successfully reproduce the key features of XMCD and RIXS-MCD spectra for epitaxial $\text{La}_{0.7}\text{Sr}_{0.3}\text{MnO}_3$ (LSMO) films, a representative itinerant ferromagnet. Our analysis highlights the crucial roles of full CT treatment, particularly in the mixed valence systems, where the conventional approaches often fail. Furthermore, we demonstrate that the CVEC effect significantly modulates the multiplet structures of the final states of XMCD and intermediate states of RIXS-MCD, leading to complex dipole selection behaviors dependent on incident X-ray photon energy. This CVEC-induced complexity greatly reduces the practicality of the XMCD sum-rule, particularly in light $3d$ systems, and emphasizes the strong photon energy dependency of the RIXS-MCD map.

In our approach, starting from the atomic model, we develop many-body calculations that include the CVEC effect. To incorporate the metallic feature of valence electrons, we employ full CT based on ligand field theory, offering a significant improvement over conventional treatments of mixed-valence systems. Our study represents an important step toward extracting accurate empirical physical parameters from spectral data, such as those from RIXS and XMCD. Moving forward, parameterizing AIM using density functional theory (DFT) and dynam-

ical mean-field theory (DMFT) methods offers a promising route for further refining our model and achieving even more precise agreement with experimental spectra [50–54]. Amalgamating two distinct approaches facilitates a more accurate reproduction of the experimental spectra. We believe our work is a significant advancement toward this goal, bridging theoretical and experimental investigations in complex correlated systems.

METHODS

Epitaxial LSMO films with 20 unit cells thick are grown on (001) SrTiO_3 single-crystal substrates via pulsed laser deposition. The laser fluence is relatively low, approximately 0.3 J/cm^2 , at the target surface with a spot size of about 10 mm^2 , and a repetition rate was 2 Hz. During the film deposition, the temperature is maintained at 800°C with an oxygen partial pressure of 5×10^{-6} Torr. After deposition, the samples are cooled down to room temperature avoiding exposure to air. Detailed growth conditions can be found in a previous publication [55]. XMCD and RIXS-MCD measurements are conducted on the films at beamline 13-3, Stanford Synchrotron Radiation Lightsource (SSRL).

The XMCD spectra are obtained in the total electron yield (TEY) mode. The X-ray absorption spectroscopy (XAS) spectra of LSMO are measured with two orthogonal polarizations: right circular polarization (RCP) and left circular polarization (LCP), under a constant magnetic field ($H \sim 0.2$ Tesla) [see the inset of Fig. 1(a)].

Traditionally, the RIXS-MCD signal is weak due to its small cross-section [21]. To address this limitation, we employ a high-efficiency superconducting transition-edge-sensor (TES) spectrometer [56]. Figure 1(b) illustrates the experimental setup for RIXS-MCD measurement using the TES under an external magnetic field ($H \sim 0.2$ Tesla). In the RIXS process, the circularly polarized X-ray photons with a photon energy of E_{in} are injected into the sample at the incident angle of 30° against the surface. Core electrons in the Mn $2p$ levels are excited to unoccupied states of the valence Mn $3d$ bands, resulting in a $2p \rightarrow 3d$ dipole transition. As the excited electrons decay, X-ray photons are emitted with a certain photon energy of E_{out} . The inelastic decay process ($\Delta E = E_{out} - E_{in} \neq 0$) enables the probing of electronic excitations such as phonon, magnon, dd , and charge-transfer (CT) excitations [20, 21].

ACKNOWLEDGMENTS

We thank K.-T. Ko, Hyeong-Do Kim, and Atsushi Hariki for the interesting discussions. B.H.K and B.K. thank the Center for Theoretical Physics of Complex Systems (IBS-PCS) Advanced Study Group program for their support during this collaboration. All soft x-ray experiments were carried out at the SSRL (beamline 13-3), SLAC National Accelerator Laboratory. This study at the SSRL/SLAC is supported by the U.S. Department of Energy, Office of Science, Office of Basic Energy Sciences under contract no. DE-AC02-76SF00515. B.H.K was supported from the Institute for Basic Science in the Republic of Korea through the Project No. IBS-R024-D1. B.K. acknowledges support from NRF Grants No. 2021R1C1C1007017, No. 2021R1A4A1031920, and No. 2022M3H4A1A04074153 and the KISTI Supercomputing Center (Project No. KSC-2022- CRE-0465). HH acknowledges support from the Science and Technology Commission of Shanghai Municipality Grant No. 21JC1400200. PA acknowledges support from the Gordon and Betty Moore Foundation's EPIQS Initiative, Grant GBMF9452.

[1] M. Coey, Charge-ordering in oxides, *Nature* **430**, 155 (2004).
 [2] J. M. D. Coey, M. Viret, and S. von Molnár, Mixed-valence manganites, *Adv. Phys.* **48**, 167 (1999).
 [3] S. Jin, T. H. Tiefel, M. McCormack, R. A. Fastnacht, R. Ramesh, and L. H. Chen, Thousandfold Change in Resistivity in Magnetoresistive La-Ca-Mn-O Films, *Science* **264**, 413 (1994).
 [4] Y. Moritomo, A. Asamitsu, H. Kuwahara, and Y. Tokura, Giant magnetoresistance of manganese oxides with a layered perovskite structure, *Nature* **380**, 141 (1996).

[5] T. Kimura, Y. Tomioka, H. Kuwahara, A. Asamitsu, M. Tamura, and Y. Tokura, Interplane Tunneling Magnetoresistance in a Layered Manganite Crystal, *Science* **274**, 1698 (1996).
 [6] T. Kimura, T. Goto, H. Shintani, K. Ishizaka, T. Arima, and Y. Tokura, Magnetic control of ferroelectric polarization, *Nature* **426**, 55 (2003).
 [7] N. Hur, S. Park, P. A. Sharma, J. S. Ahn, S. Guha, and S. W. Cheong, Electric polarization reversal and memory in a multiferroic material induced by magnetic fields, *Nature* **429**, 392 (2004).
 [8] J. G. Bednorz and K. A. Müller, Possible high T_c superconductivity in the Ba-La-Cu-O system, *Z. Phys. B Condens. Matter* **64**, 189 (1986).
 [9] B. Keimer, S. A. Kivelson, M. R. Norman, S. Uchida, and J. Zaanen, From quantum matter to high-temperature superconductivity in copper oxides, *Nature* **518**, 179 (2015).
 [10] B. J. Kim, H. Jin, S. J. Moon, J.-Y. Kim, B.-G. Park, C. S. Leem, J. Yu, T. W. Noh, C. Kim, S.-J. Oh, J.-H. Park, V. Durairaj, G. Cao, and E. Rotenberg, Novel $J_{\text{eff}} = 1/2$ Mott State Induced by Relativistic Spin-Orbit Coupling in Sr_2IrO_4 , *Phys. Rev. Lett.* **101**, 076402 (2008).
 [11] B. J. Kim, H. Ohsumi, T. Komesu, S. Sakai, T. Morita, H. Takagi, and T. Arima, Phase-Sensitive Observation of a Spin-Orbital Mott State in Sr_2IrO_4 , *Science* **323**, 1329 (2009).
 [12] A. M. Oleś, K. Wohlfeld, and G. Khaliullin, Orbital Symmetry and Orbital Excitations in High- T_c Superconductors, *Condens. Matter* **4**, 46 (2019).
 [13] J.-S. Lee, Y. W. Xie, H. K. Sato, C. Bell, Y. Hikita, H. Y. Hwang, and C.-C. Kao, Titanium d_{xy} ferromagnetism at the $\text{LaAlO}_3/\text{SrTiO}_3$ interface, *Nat. Mater.* **12**, 703 (2013).
 [14] M. Salluzzo, J. C. Cezar, N. B. Brookes, V. Bisogni, G. M. De Luca, C. Richter, S. Thiel, J. Mannhart, M. Huijben, A. Brinkman, G. Rijnders, and G. Ghiringhelli, Orbital Reconstruction and the Two-Dimensional Electron Gas at the $\text{LaAlO}_3/\text{SrTiO}_3$ Interface, *Phys. Rev. Lett.* **102**, 166804 (2009).
 [15] G. van der Laan, B. T. Thole, G. A. Sawatzky, J. B. Goedkoop, J. C. Fuggle, J.-M. Esteve, R. Karnatak, J. P. Remeika, and H. A. Dabkowska, Experimental proof of magnetic x-ray dichroism, *Phys. Rev. B* **34**, 6529 (1986).
 [16] J. Stöhr, Exploring the microscopic origin of magnetic anisotropies with X-ray magnetic circular dichroism (XMCD) spectroscopy, *J Magn. Magn. Mater.* **200**, 470 (1999).
 [17] C. T. Chen, Y. U. Idzerda, H.-J. Lin, N. V. Smith, G. Meigs, E. Chaban, G. H. Ho, E. Pellegrin, and F. Sette, Experimental Confirmation of the X-Ray Magnetic Circular Dichroism Sum Rules for Iron and Cobalt, *Phys. Rev. Lett.* **75**, 152 (1995).
 [18] B. T. Thole, P. Carra, F. Sette, and G. van der Laan, X-ray circular dichroism as a probe of orbital magnetization, *Phys. Rev. Lett.* **68**, 1943 (1992).
 [19] P. Carra, B. T. Thole, M. Altarelli, and X. Wang, X-ray circular dichroism and local magnetic fields, *Phys. Rev. Lett.* **70**, 694 (1993).
 [20] A. Kotani and S. Shin, Resonant inelastic x-ray scattering spectra for electrons in solids, *Rev. Mod. Phys.* **73**, 203 (2001).
 [21] L. J. P. Ament, M. van Veenendaal, T. P. Devereaux,

- J. P. Hill, and J. van den Brink, Resonant inelastic x-ray scattering studies of elementary excitations, *Rev. Mod. Phys.* **83**, 705 (2011).
- [22] P. Strange, P. J. Durham, and B. L. Gyorffy, Dichroic x-ray fluorescence, *Phys. Rev. Lett.* **67**, 3590 (1991).
- [23] L.-C. Duda, J. Stöhr, D. C. Mancini, A. Nilsson, N. Wassdahl, J. Nordgren, and M. G. Samant, Magnetic dichroism in $L_{2,3}$ emission of Fe, Co, and Ni following energy-dependent excitation with circularly polarized x rays, *Phys. Rev. B* **50**, 16758 (1994).
- [24] M. V. Yablonskikh, Y. M. Yarmoshenko, V. I. Grebennikov, E. Z. Kurmaev, S. M. Butorin, L.-C. Duda, J. Nordgren, S. Plogmann, and M. Neumann, Origin of magnetic circular dichroism in soft x-ray fluorescence of Heusler alloys at threshold excitation, *Phys. Rev. B* **63**, 235117 (2001).
- [25] L. Braicovich, G. van der Laan, G. Ghiringhelli, A. Tagliaferri, M. A. van Veenendaal, N. B. Brookes, M. M. Chervinskii, C. Dallera, B. De Michelis, and H. A. Dürr, Magnetic Circular Dichroism in Resonant Raman Scattering in the Perpendicular Geometry at the L edge of $3d$ Transition Metal Systems, *Phys. Rev. Lett.* **82**, 1566 (1999).
- [26] J. Miyawaki, S. Suga, H. Fujiwara, H. Niwa, H. Kiuchi, and Y. Harada, A compact permanent-magnet system for measuring magnetic circular dichroism in resonant inelastic soft X-ray scattering, *J. Synchrotron Rad.* **24**, 449 (2017).
- [27] T. Inami, Magnetic Circular Dichroism in X-Ray Emission from Ferromagnets, *Phys. Rev. Lett.* **119**, 137203 (2017).
- [28] W. L. O'Brien and B. P. Tonner, Orbital and spin sum rules in x-ray magnetic circular dichroism, *Phys. Rev. B* **50**, 12672 (1994).
- [29] D. Weller, J. Stöhr, R. Nakajima, A. Carl, M. G. Samant, C. Chappert, R. Mégy, P. Beauvillain, P. Veillet, and G. A. Held, Microscopic Origin of Magnetic Anisotropy in Au/Co/Au Probed with X-Ray Magnetic Circular Dichroism, *Phys. Rev. Lett.* **75**, 3752 (1995).
- [30] Y. Wu, J. Stöhr, B. D. Hermsmeier, M. G. Samant, and D. Weller, Enhanced orbital magnetic moment on Co atoms in Co/Pd multilayers: A magnetic circular x-ray dichroism study, *Phys. Rev. Lett.* **69**, 2307 (1992).
- [31] R. Nakajima, J. Stöhr, and Y. U. Idzerda, Electron-yield saturation effects in L-edge x-ray magnetic circular dichroism spectra of Fe, Co, and Ni, *Phys. Rev. B* **59**, 6421 (1999).
- [32] G. Jonker and J. Van Santen, Ferromagnetic compounds of manganese with perovskite structure, *Physica* **16**, 337 (1950).
- [33] Y. Tokura, A. Urushibara, Y. Moritomo, T. Arima, A. Asamitsu, G. Kido, and N. Furukawa, Giant Magnetotransport Phenomena in Filling-Controlled Kondo Lattice System: $\text{La}_{1-x}\text{Sr}_x\text{MnO}_3$, *J. Phys. Soc. Jpn.* **63**, 3931 (1994).
- [34] J.-H. Park, E. Vescovo, H.-J. Kim, C. Kwon, R. Ramesh, and T. Venkatesan, Direct evidence for a half-metallic ferromagnet, *Nature* **392**, 794 (1998).
- [35] F. de Groot, Multiplet effects in X-ray spectroscopy, *Coord. Chem. Rev.* **249**, 31 (2005).
- [36] E. Stavitski and F. M. F. de Groot, The CTM4XAS program for EELS and XAS spectral shape analysis of transition metal L edges, *Micron* **41**, 687 (2010).
- [37] R. Boca, *Theoretical foundations of molecular magnetism* (Elsevier, 1999).
- [38] K. Wu and H. Simon, Thick-Restart Lanczos Method for Large Symmetric Eigenvalue Problems, *SIAM J. Matrix Anal. Appl.* **22**, 602 (2000).
- [39] P. Yu, J.-S. Lee, S. Okamoto, M. D. Rossell, M. Huijben, C.-H. Yang, Q. He, J. X. Zhang, S. Y. Yang, M. J. Lee, Q. M. Ramasse, R. Erni, Y.-H. Chu, D. A. Arena, C.-C. Kao, L. W. Martin, and R. Ramesh, Interface Ferromagnetism and Orbital Reconstruction in $\text{BiFeO}_3\text{-La}_{0.7}\text{Sr}_{0.3}\text{MnO}_3$ Heterostructures, *Phys. Rev. Lett.* **105**, 027201 (2010).
- [40] J.-S. Lee, D. A. Arena, P. Yu, C. S. Nelson, R. Fan, C. J. Kinane, S. Langridge, M. D. Rossell, R. Ramesh, and C.-C. Kao, Hidden Magnetic Configuration in Epitaxial $\text{La}_{1-x}\text{Sr}_x\text{MnO}_3$ Films, *Phys. Rev. Lett.* **105**, 257204 (2010).
- [41] J. Stöhr and H. König, Determination of Spin- and Orbital-Moment Anisotropies in Transition Metals by Angle-Dependent X-Ray Magnetic Circular Dichroism, *Phys. Rev. Lett.* **75**, 3748 (1995).
- [42] R. Wu and A. J. Freeman, Limitation of the Magnetic-Circular-Dichroism Spin Sum Rule for Transition Metals and Importance of the Magnetic Dipole Term, *Phys. Rev. Lett.* **73**, 1994 (1994).
- [43] G. van der Laan, K. T. Moore, J. G. Tobin, B. W. Chung, M. A. Wall, and A. J. Schwartz, Applicability of the Spin-Orbit Sum Rule for the Actinide $5f$ States, *Phys. Rev. Lett.* **93**, 097401 (2004).
- [44] C. Piamonteze, P. Miedema, and F. M. F. de Groot, Accuracy of the spin sum rule in XMCD for the transition-metal L edges from manganese to copper, *Phys. Rev. B* **80**, 184410 (2009).
- [45] C. Piamonteze, P. Miedema, and F. M. F. de Groot, The accuracy of the spin sum rule in XMCD, *J. Phys. Conf. Ser.* **190**, 012015 (2009).
- [46] G. Ghiringhelli, N. B. Brookes, E. Annese, H. Berger, C. Dallera, M. Grioni, L. Perfetti, A. Tagliaferri, and L. Braicovich, Low Energy Electronic Excitations in the Layered Cuprates Studied by Copper L_3 Resonant Inelastic X-Ray Scattering, *Phys. Rev. Lett.* **92**, 117406 (2004).
- [47] G. Ghiringhelli, M. Matsubara, C. Dallera, F. Fracassi, A. Tagliaferri, N. B. Brookes, A. Kotani, and L. Braicovich, Resonant inelastic x-ray scattering of MnO: $L_{2,3}$ edge measurements and assessment of their interpretation, *Phys. Rev. B* **73**, 035111 (2006).
- [48] H. J. Lee, G. Kim, D. H. Kim, J.-S. Kang, C. L. Zhang, S.-W. Cheong, J. H. Shim, S. Lee, H. Lee, J.-Y. Kim, B. H. Kim, and B. I. Min, Valence states and occupation sites in $(\text{fe,mn})_3\text{o}_4$ spinel oxides investigated by soft x-ray absorption spectroscopy and magnetic circular dichroism, *J. Phys. Condens. Matter* **20**, 295203 (2008).
- [49] J. Lee, B. Kim, B. H. Kim, B. I. Min, S. Kolesnik, O. Chmaissem, J. Mais, B. Dabrowski, H. J. Shin, D. H. Kim, H. J. Lee, and J.-S. Kang, Valence-state transition in $\text{SrMn}_{1-x}\text{Mo}_x\text{O}_3$ ($0 \leq x \leq 0.5$) investigated by soft x-ray absorption spectroscopy, *Phys. Rev. B* **80**, 205112 (2009).
- [50] M. W. Haverkort, Quanta for core level spectroscopy - excitons, resonances and band excitations in time and frequency domain, *J. Phys.: Conf. Ser.* **712**, 012001 (2016).
- [51] A. Hariki, M. Winder, and J. Kuneš, Continuum Charge Excitations in High-Valence Transition-Metal Oxides Revealed by Resonant Inelastic X-Ray Scattering, *Phys.*

- Rev. Lett.* **121**, 126403 (2018).
- [52] Y. Wang, G. Fabbris, M. Dean, and G. Kotliar, EDRIXS: An open source toolkit for simulating spectra of resonant inelastic x-ray scattering, *Comput. Phys. Commun.* **243**, 151 (2019).
- [53] A. Hariki, M. Winder, T. Uozumi, and J. Kuneš, LDA + DMFT approach to resonant inelastic x-ray scattering in correlated materials, *Phys. Rev. B* **101**, 115130 (2020).
- [54] M. W. Haverkort, M. Zwierzycki, and O. K. Andersen, Multiplet ligand-field theory using Wannier orbitals, *Phys. Rev. B* **85**, 165113 (2012).
- [55] J. H. Song, T. Susaki, and H. Y. Hwang, Enhanced Thermodynamic Stability of Epitaxial Oxide Thin Films, *Adv. Mater.* **20**, 2528 (2008).
- [56] W. B. Doriese, P. Abbamonte, B. K. Alpert, D. A. Bennett, E. V. Denison, Y. Fang, D. A. Fischer, C. P. Fitzgerald, J. W. Fowler, J. D. Gard, J. P. Hays-Wehle, G. C. Hilton, C. Jaye, J. L. McChesney, L. Miaja-Avila, K. M. Morgan, Y. I. Joe, G. C. O'Neil, C. D. Reintsema, F. Rodolakis, D. R. Schmidt, H. Tatsuno, J. Uhlig, L. R. Vale, J. N. Ullom, and D. S. Swetz, A practical superconducting-microcalorimeter X-ray spectrometer for beamline and laboratory science, *Rev. Sci. Instrum.* **88**, 053108 (2017).

**SUPPLEMENTARY MATERIALS:
X-RAY MAGNETIC CIRCULAR DICHROISM
AND RESONANT INELASTIC X-RAY
SCATTERING EXPLAINED:
ROLE OF MANY-BODY CORRELATION AND
MIXED-VALENCE FLUCTUATIONS**

Charge Transfer effect

Figure S1 presents the partial density of states with various electronic configurations and average number of holes at the Mn site for the ground state, where we have systematically changed the hopping strengths between $3d$ and ligand orbitals. Here, we have defined the scale parameter r which tunes the hopping strengths: $V_{pd\sigma} = -2 \times r$ and $V_{pd\pi} = 1 \times r$ eV. For example, in the case of $r = 0$, there is no d - p overlap, and the ground state is solely determined by states with d^3 configuration. Hence, the average number of holes is 7. When r increases starting from $r = 0$, electrons can dynamically transfer from ligand (bath) to Mn sites. The contribution from other states besides d^3 configurations contributes to the ground state and the number of holes decreases monotonically. Upon increasing the hopping strengths, more electrons move from the ligand to Mn sites, and when r is about 0.6, transferred electron numbers reaches to 0.7. Then d^4L^1 configuration contributes more to the ground state than d^3 configuration. The actual LSMO case corresponds to the $r > 0.6$ in the calculation. In the calculation, we set $r = 1$. In this case, the averaged number of holes at the Mn site in the ground state is calculated to be about 6.1, slightly deviating from the nominal value of 6.3. We validate our calculations by comparing the electronic structures of the AIM with those from mean-field density functional theory calculation as in the next section.

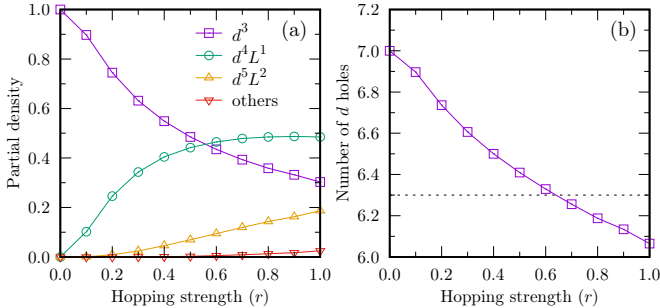


FIG. S1. (a) The partial density of states with various electronic configurations for the ground state and (b) average number of holes at the Mn site a function of the scale parameter r of hopping strength. r is defined as $V_{pd\sigma} = -2 \times r$ and $V_{pd\pi} = 1 \times r$ eV.

Electronic structure

To check the validity of our AIM calculation, we explore the electronic structures and compare them with those from the mean-field density functional theory (DFT) calculation. To obtain the density of states (DOSs) from AIM, we first calculated the one-particle Green function for a given frequency point z , which is expressed as follows:

$$G_{\alpha\beta}(z) = \langle \Psi_g | d_\alpha \frac{1}{z - H + E_g - \mu_c} d_\beta^\dagger | \Psi_g \rangle + \langle \Psi_g | d_\beta^\dagger \frac{1}{z + H - E_g - \mu_c} d_\alpha | \Psi_g \rangle, \quad (\text{S1})$$

where d_α (d_α^\dagger) is the annihilation (creation) operator of valence α states and $|\Psi_g\rangle$, E_g , and μ_c are the ground state, ground energy, and chemical potential, respectively. μ_c is determined from the Fermi level, which is to be located between electron and hole bands. The partial DOS of α state can be computed by $A_\alpha(\omega) = -\frac{1}{\pi} \text{Im} G_{\alpha\alpha}(\omega + i\delta_b)$, where δ_b being the broadening parameter. The DFT calculations were performed employing the Vienna ab initio simulation package (VASP). We utilized SCAN (strongly constrained and appropriately normed semilocal) functional employing the realistic supercell of $\text{La}_{3/4}\text{Sr}_{1/4}\text{MnO}_3$ with eight formula units. The

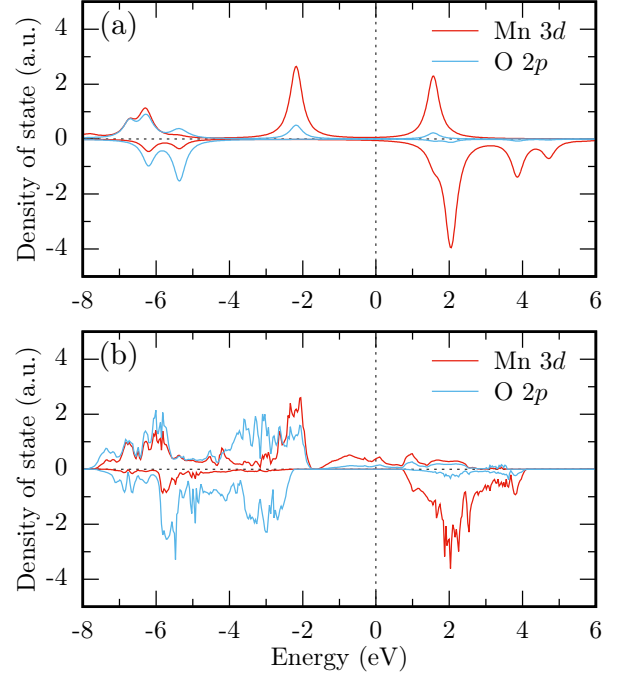


FIG. S2. The partial density of states calculated by (a) the Anderson impurity model (AIM) calculation and (b) the density functional theory calculation with the SCAN functional. The Fermi level is denoted by the vertical dotted lines. Parameters for the AIM are the same in the main manuscript.

energy cut for the plane waves is 400 eV and Monkhorst-Pack k -mesh of $4 \times 4 \times 4$ was used.

Figure S2 present the partial DOS calculated from the AIM and DFT. We can clearly see that our AIM result qualitatively captures the main features of the DFT calculations: i) the bonding bands of Mn- $3d$ and O- $2p$ orbitals are spread over -7 – -5 eV, ii) spin-up antibonding bands are located at around -2 eV, and iii) the unoccupied spin-down bands of Mn- $3d$ orbitals have main peak at around 2 eV with subpeak at 4 eV. Even though some details such as metallic bands at Fermi level and non-bonding O- $2p$ bands at around -5 – -2 eV are different due to finite-size cluster limits, the essential features are well-captured from our AIM. And we believe that the AIM calculation is capable to simulate the excitation spectra of LSMO with large energy scale ranges of about 10 eV.

XAS calculation

Let $|\Psi_g\rangle$ be a ground state with energy E_g . The XAS intensity for the circularly polarized X-ray photon μ_m ($m = \pm 1, 0$) is calculated with the following equation:

$$\mu_m = -\frac{1}{\pi} \text{Im} \langle \Psi_g | \hat{e}_{-m} \cdot \mathbf{D}^\dagger \frac{1}{E_{\text{in}} - H + E_g + i\delta_{\text{in}}} \hat{e}_m \cdot \mathbf{D} | \Psi_g \rangle, \quad (\text{S2})$$

where E_{in} is energy of incident x-ray with broadening δ_{in} . \hat{e}_m is the x-ray polarization vector defined as $\hat{e}_{\pm 1} = \frac{1}{\sqrt{2}}(\hat{x} \pm i\hat{y})$ and $\hat{e}_0 = \hat{z}$, and \mathbf{D} is the dipole operator given as

$$\mathbf{D} = \sum_{\alpha m \sigma} \langle \psi_\alpha^d | \mathbf{r} | \psi_m^c \rangle d_{\alpha\sigma}^\dagger c_{p\sigma}, \quad (\text{S3})$$

$$I_{\text{RIXS}}(\omega, \mathbf{q}, \boldsymbol{\epsilon}, \boldsymbol{\epsilon}') = -\frac{1}{\pi} \text{Im} \langle \Psi(E_{\text{in}}, \mathbf{q}, \boldsymbol{\epsilon}, \boldsymbol{\epsilon}') | \frac{1}{\omega - H + E_g + i\delta_b} | \Psi(E_{\text{in}}, \mathbf{q}, \boldsymbol{\epsilon}, \boldsymbol{\epsilon}') \rangle, \quad (\text{S7})$$

where δ_b is the broadening parameter for the RIXS spectra. Here, we set $\delta_{\text{in}} = \delta_b = 0.3$ eV. We utilize the Lanczos method to solve the RIXS intensity in Eq. S7, and the complex-shifted minimal residual method to solve for the state in Eq. S6.

In the AIM calculation, we set $\mathbf{q} = 0$ and obtain the RIXS intensity for the circularly polarized incident X-

ray photon ($m = \pm 1$) as follows:

$$I_{\text{RIXS}}^m(\omega) = I_{\text{RIXS}}(\omega, \boldsymbol{\epsilon}_m, \boldsymbol{\epsilon}'_+) + I_{\text{RIXS}}(\omega, \boldsymbol{\epsilon}_m, \boldsymbol{\epsilon}'_-) \quad (\text{S8})$$

where $d_{\alpha\sigma}^\dagger$ and $d_{\alpha\sigma}$ ($c_{p\sigma}^\dagger$ and $c_{p\sigma}$) are the creation and annihilation operators of valence $3d$ (core $2p$) orbitals with a wave function ψ_α^d (ψ_p^c) and spin σ . Then, XAS and XMCD intensities are obtained from $\mu = \mu_{+1} + \mu_{-1}$ and $\Delta\mu = \mu_{+1} - \mu_{-1}$, respectively.

RIXS calculation

The RIXS spectrum is derived using the Kramers-Heisenberg equation:

$$I_{\text{RIXS}}(\omega, \mathbf{q}, \boldsymbol{\epsilon}, \boldsymbol{\epsilon}') = \sum_f |\mathcal{F}_{fg}(E_{\text{in}}, \mathbf{q}, \boldsymbol{\epsilon}, \boldsymbol{\epsilon}')|^2 \delta(\omega - E_f + E_g), \quad (\text{S4})$$

where $\omega = E_{\text{in}} - E_{\text{out}} = -\Delta E$, $\mathbf{q} = \mathbf{k}' - \mathbf{k}$, and E_g and E_f are energies of ground and excitation states, respectively [21]. Here, \mathbf{k} (\mathbf{k}'), E_{in} (E_{out}), and $\boldsymbol{\epsilon}$ ($\boldsymbol{\epsilon}'$) refer to the momentum, energy, and polarization of an incident (outgoing) X-ray photon, respectively. Under the dipole approximation, the function \mathcal{F}_{fg} is expressed as:

$$\mathcal{F}_{fg}(E_{\text{in}}, \mathbf{q}, \boldsymbol{\epsilon}, \boldsymbol{\epsilon}') = \sum_j e^{i\mathbf{q}\cdot\mathbf{r}_j} \langle \Psi_f | \boldsymbol{\epsilon}'^* \cdot \mathbf{D}_j^\dagger \frac{1}{E_g + E_{\text{in}} - H + i\delta_{\text{in}}} \boldsymbol{\epsilon} \cdot \mathbf{D}_j | \Psi_g \rangle, \quad (\text{S5})$$

where \mathbf{r}_j and \mathbf{D}_j are the position vector and dipole operator of the j th Mn ion, respectively. δ_{in} is the broadening parameter of an incident X-ray photon. The state $|\Psi(E_{\text{in}}, \mathbf{q}, \boldsymbol{\epsilon}, \boldsymbol{\epsilon}')\rangle$ can be expressed as:

$$|\Psi(E_{\text{in}}, \mathbf{q}, \boldsymbol{\epsilon}, \boldsymbol{\epsilon}')\rangle = \sum_j e^{i\mathbf{q}\cdot\mathbf{r}_j} \boldsymbol{\epsilon}'^* \cdot \mathbf{D}_j^\dagger \frac{1}{E_g + E_{\text{in}} - H + i\delta_{\text{in}}} \boldsymbol{\epsilon} \cdot \mathbf{D}_j | \Psi_g \rangle. \quad (\text{S6})$$

Now, the RIXS intensity, $I_{\text{RIXS}}(\omega, \mathbf{q}, \boldsymbol{\epsilon}, \boldsymbol{\epsilon}')$, can be calculated from:

raya photon ($m = \pm 1$) as follows:

$$I_{\text{RIXS}}^m(\omega) = I_{\text{RIXS}}(\omega, \boldsymbol{\epsilon}_m, \boldsymbol{\epsilon}'_+) + I_{\text{RIXS}}(\omega, \boldsymbol{\epsilon}_m, \boldsymbol{\epsilon}'_-) \quad (\text{S8})$$

in the experimental geometry as shown in Fig. 1(b) in the main text. The RIXS and RIXS-MCD intensities are calculated as $I_{\text{RIXS}} = I_{\text{RIXS}}^+ + I_{\text{RIXS}}^-$ and $I_{\text{RIXS-MCD}} = I_{\text{RIXS}}^+ - I_{\text{RIXS}}^-$, respectively.

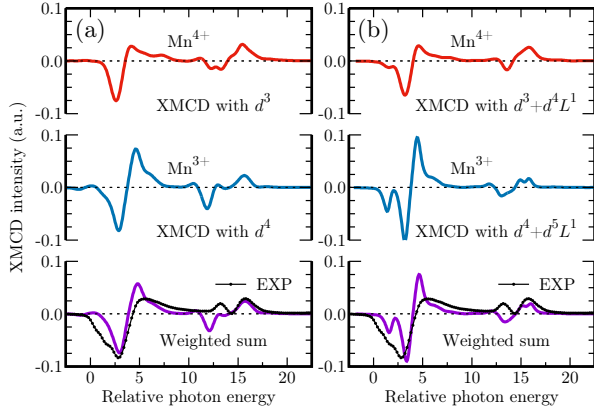


FIG. S3. The X-ray magnetic circular dichroism (XMCD) intensities of Mn^{4+} , Mn^{3+} , and their weighted sum (30% contribution of Mn^{4+} and 70% contribution of Mn^{3+}) are presented with (a) no charge transfer (CT) states and (b) CT states, i.e., d^4L^1 states for Mn^{4+} and d^5L^1 states for Mn^{3+} . All results are obtained by the CTM4XAS software [36].

Weighted sum from conventional cluster calculation

To compare our XMCD results with conventional approaches for mixed-valence states, we perform calculations using the CTM4XAS software [36]. First, we calculate the XMCD spectra for Mn^{4+} with a d^3 configuration and Mn^{3+} with a d^4 configuration separately. We then take a weighted sum of the spectra, with 30% contribution from Mn^{4+} and 70% from Mn^{3+} , representing the mixed-valence state of $\text{La}_{0.7}\text{Sr}_{0.3}\text{MnO}_3$. As shown in Fig. S3(a), this approach fails to reproduce the extended subpeak structures in the L_3 -edge at the relative photon energy of around $0 \sim 2$ eV and the positive XMCD signal in the L_2 edge at $13 \sim 14$ eV regime. Next, we incorporate the CT effect into the calculation by adding the CT states: d^4L^1 for Mn^{4+} and d^5L^1 for Mn^{3+} . Similarly, we take the weighted sum of the resulting spectra. These results, presented in Fig. S3(b), also fail to reproduce the extended subpeak structures at the L_3 -edge and the distinctive positive two-peak structure at the L_2 -edge observed in the experimental XMCD spectra. Therefore, the conventional approaches, even with the inclusion of the CT effect of $d^{n+1}L^1$ configuration, are inadequate in capturing the consistent XMCD features observed experimentally.

Partial excitation density distribution

To explore the intermediate and final states involved in XAS and RIXS processes, we compute the partial excitation density (PED) distribution of multiplet states with specific configurations such as $t_{2g\uparrow}^3$, $t_{2g\uparrow}^2e_{g\downarrow}$, $t_{2g\uparrow}^3e_{g\uparrow}L^1$,

$t_{2g\uparrow}^3e_{g\uparrow}c^1$, and so on, where L and c represent ligand (bath) hole and Mn core $2p$ hole orbitals, respectively.

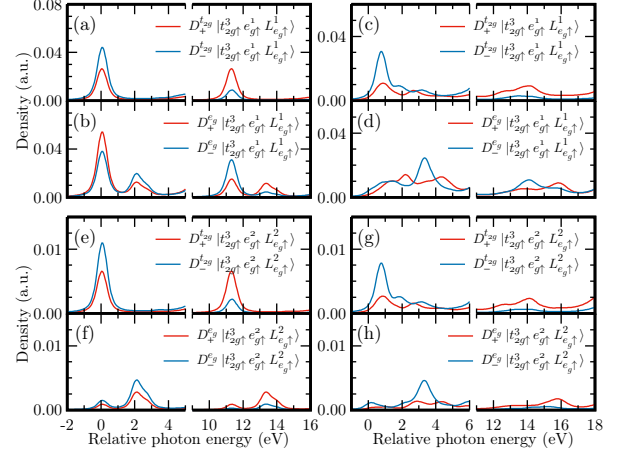


FIG. S4. The partial excitation distribution behaviors of multiplet states derived from (a)–(d) $|t_{2g\uparrow}^3e_{g\uparrow}^1L_{e_g\uparrow}^1\rangle$ and (e)–(f) $|t_{2g\uparrow}^3e_{g\uparrow}^2L_{e_g\uparrow}^2\rangle$ through the dipole transition operators of $D_+^{t_{2g}}$ and D_+^{e} . c and $L_{e_g\uparrow}$ denote the core-hole orbital and ligand (bath) hole orbital with the e_g orbital symmetry and \uparrow spin state, respectively. The scale parameter of core-valence exchange correlations s is set by $s = 0$ for (a), (b), (e), and (f), and $s = 1$ for (c), (d), (g), and (h), respectively. The scale parameter s is defined as $F_{pd}^2 = 5.7508 \times s$, $G_{pd}^1 = 4.2864 \times s$, and $G_{pd}^3 = 2.4382 \times s$ eV. Colored arrows refer to the peak positions of XMCD spectra. Other parameters are presented in the main manuscript.

Let $|\Phi_l^\xi\rangle$ denote the l th state for a given ξ configuration. The partial excitation density $\Lambda_\xi(\omega)$ is calculated as follows:

$$\Lambda_\xi(\omega) = \sum_n \sum_l \left| \langle \Psi_n | \Phi_l^\xi \rangle \right|^2 \delta(\omega - E_n + E_g) \\ = -\frac{1}{\pi} \text{Im} \sum_l \langle \Phi_l^\xi | \frac{1}{\omega - H + E_g + i\delta_b} | \Phi_l^\xi \rangle, \quad (\text{S9})$$

where E_n and Ψ_n are the energy and eigenstate of the n th state, respectively, and E_g is the ground state energy. We set the broadening parameter δ_b to be 0.3 eV. We utilize the Lanczos method to solve this equation.

The XMCD contribution of the CT states

To analyze the XMCD spectra, we calculate the PED distribution of the final XMCD states derived from the CT states $|t_{2g\uparrow}^3e_{g\uparrow}^1L_{e_g\uparrow}^1\rangle$ and $|t_{2g\uparrow}^3e_{g\uparrow}^2L_{e_g\uparrow}^2\rangle$, which mainly constitute the ground multiplet state, through the dipole transition operators of $D_+^{t_{2g}}$ and D_+^{e} . Results are presented in Fig. S4.